Acta Cryst. (1997). A53, 46–54

Bragg Reflection in Mosaic Crystals. II. Neutron Monochromator Properties

V. F. SEARS

Atomic Energy of Canada Limited, Chalk River Laboratories, Chalk River, Ontario, Canada K0J 1J0. E-mail: searsv@aecl.ca

(Received 24 April 1996; accepted 2 August 1996)

Abstract

In the preceding article, the general solution of the Darwin equations has been obtained for a mosaic crystal slab for both the Laue case (transmission geometry) and the Bragg case (reflection geometry). This now allows the calculation, for the first time, of the reflectivity of an absorbing crystal of finite thickness in situations where the Bragg planes make an arbitrary angle with the surface of the crystal. In this paper, these results are applied to a numerical calculation of the reflecting properties of a number of commonly used neutron monochromator crystals. The incident-neutron flux is taken to be Maxwellian with an epithermal tail and it is investigated how the various properties depend on the neutron wavelength, the crystal thickness, the mosaic spread and the angle that the Bragg planes make with the surface of the crystal. It is found, for example, that for asymmetrical reflections gains in flux of 25 to 50% or more can easily be achieved for a wide range of wavelengths in crystals with the kinds of thickness and mosaic spread that are available in practice.

1. Introduction

In the preceding article (Sears, 1997, hereafter referred to as paper I), we have obtained the general solution of the Darwin equations for a mosaic crystal slab for both the Laue case (transmission geometry) and the Bragg case (reflection geometry). This now allows us, for the first time, to calculate the reflectivity of an absorbing crystal of finite thickness in situations where the Bragg planes make an arbitrary angle with the surface of the crystal. In this paper, we apply these results to a numerical calculation of the reflecting properties of a number of commonly used neutron monochromator crystals: aluminium, copper, germanium, silicon, beryllium and pyrolytic graphite.

In particular, we have calculated the following quantities: reflectivity, figure of merit, reflected flux, optimum thickness, order contamination and Fankuchen gain. The incident-neutron flux has been taken to be Maxwellian with an epithermal tail and the effective neutron temperature was chosen to simulate both a thermal source and a cold source. The attenuation coefficient included contributions from true absorption (*e.g.* radiative capture), incoherent scattering and coherent inelastic scattering. The quantities listed above have been calculated for the most commonly used Bragg planes (*hkl*) and we have investigated how they depend on the neutron wavelength λ, the crystal thickness d, the mosaic spread $\Delta\theta$ and the angle α that the Bragg planes make with the surface of the crystal. For asymmetric reflections (where $0 < \alpha < 90°$), we have examined both compression and expansion geometries. Owing to space limitations, we cannot report all these results in detail but we present a representative selection that illustrates the general features of the results that we have found.

Neutron monochromator crystals are normally used with symmetrical reflection geometries where the Bragg planes are either parallel or perpendicular to the surface of the crystal. We find that for asymmetrical reflections, with α in the range 10 to 30°, gains in flux of 25 to 50% or more can easily be achieved for a wide range of wavelengths in crystals with the kinds of thickness and mosaic spread that are available in practice. Previous theoretical studies of this effect have been confined to infinitely thick crystals and the effect of secondary extinction on the gain was neglected.

2. Bragg reflection in monochromators

We begin in this section with a brief phenomenological discussion of the Bragg reflection of neutrons from a monochromator crystal in order to derive expressions for the quantities of interest in terms of the reflectivity that was calculated in I.

2.1. *Incident beam*

In I, we assumed that a collimated monoenergetic beam of neutrons was incident on the crystal. We now relax this assumption by considering a collimated polyenergetic beam. Then the total incident-neutron current (neutrons s^{-1}) can be expressed as

$$I = \int_0^\infty i(\lambda)\,\mathrm{d}\lambda, \tag{1}$$

in which $i(\lambda)\,\mathrm{d}\lambda$ is the incident-neutron current in $\mathrm{d}\lambda$. The corresponding incident-neutron flux (neutrons $\mathrm{cm}^{-2}\,\mathrm{s}^{-1}$) can be expressed similarly as

$$J = \int_0^\infty j(\lambda)\,\mathrm{d}\lambda, \tag{2}$$

so that, if S is the cross-sectional area of the incident beam,

$$i(\lambda) = Sj(\lambda), \quad I = SJ. \tag{3}$$

Finally, the incident-neutron spectrum will be defined as

$$f(\lambda) = i(\lambda)/I = j(\lambda)/J. \tag{4}$$

Then, $f(\lambda)\,\mathrm{d}\lambda$ is the fraction of incident neutrons in $\mathrm{d}\lambda$ and has the normalization property

$$\int_0^\infty f(\lambda)\,\mathrm{d}\lambda = 1. \tag{5}$$

2.2. *Bragg reflected beam*

If the incident beam makes an angle θ with the Bragg planes then the reflected-neutron current can be expressed as

$$I'(\theta) = \int_0^\infty i'(\theta, \lambda)\,\mathrm{d}\lambda \tag{6}$$

and the reflected-neutron flux as

$$J'(\theta) = \int_0^\infty j'(\theta, \lambda)\,\mathrm{d}\lambda. \tag{7}$$

As in (3),

$$i'(\theta, \lambda) = S'j'(\theta, \lambda), \quad I'(\theta) = S'J'(\theta), \tag{8}$$

in which S' denotes the cross-sectional area of the Bragg-reflected beam.

2.3. *Reflectivity*

The reflectivity $R(\theta, \lambda)$ is defined as the fraction of incident neutrons of wavelength λ that are Bragg reflected when the incident beam makes an angle θ with the Bragg planes. Thus,

$$R(\theta, \lambda) = i'(\theta, \lambda)/i(\lambda) = (1/\varsigma)\, j'(\theta, \lambda)/j(\lambda). \tag{9}$$

Here, ς is the Fankuchen factor,

$$\varsigma = S/S' = \sin\varphi/\sin\varphi', \tag{10}$$

in which φ denotes the angle that the incident beam makes with the surface of the crystal and φ' the corresponding angle for the reflected beam (see Fig. 1 in I). The net reflectivity is then given by

$$I'(\theta)/I = \int_0^\infty R(\theta, \lambda) f(\lambda)\,\mathrm{d}\lambda \tag{11}$$

and the corresponding flux ratio by

$$J'(\theta)/J = \varsigma \int_0^\infty R(\theta, \lambda) f(\lambda)\,\mathrm{d}\lambda. \tag{12}$$

The preceding equations are all essentially definitions. The physics is contained in the Darwin equations, which show (*a*) that the reflectivity $R(\theta, \lambda)$, as defined by (9), is an intrinsic property of the crystal, independent of the incident beam, and (*b*) that $R(\theta, \lambda)$ is different from zero only if λ and θ satisfy Bragg's law to within the range of values allowed by the mosaic spread in the crystal. In short,

$$R(\theta, \lambda) = 0 \quad \text{unless } \lambda \simeq \lambda_{\max} \sin\theta, \tag{13}$$

where

$$\lambda_{\max} = 4\pi/K_{hkl}, \tag{14}$$

in which K_{hkl} denotes the magnitude of the reciprocal-lattice vector for the Bragg planes (*hkl*) under consideration.

In what follows, λ and θ will continue to denote an arbitrary wavelength and Bragg angle, while λ_0 and θ_0 will represent a pair of values that satisfy Bragg's law exactly:

$$\lambda_0 = \lambda_{\max} \sin\theta_0. \tag{15}$$

2.4. *Rocking curve*

Suppose we have a collimated monoenergetic incident beam of neutrons with wavelength λ_0. Then,

$$f(\lambda) = \delta(\lambda - \lambda_0). \tag{16}$$

It now follows from (11) that

$$I'(\theta)/I = R(\theta, \lambda_0) \tag{17}$$

and from (12) that

$$J'(\theta)/J = \varsigma R(\theta, \lambda_0). \tag{18}$$

The relation (17) is just the rocking curve for the reflection *hkl* and the reflectivity $R(\theta, \lambda_0)$ can be calculated from the solution of the Darwin equations given in I. For qualitative purposes, we can think of the reflectivity as being sharply peaked at $\theta = \theta_0$ with a maximum value given by

$$R_0 = R(\theta_0, \lambda_0). \tag{19}$$

The integrated reflectivity is then defined as

$$\rho(\lambda_0) = \int R(\theta, \lambda_0)\,\mathrm{d}\theta = R_0\,\Delta\theta, \tag{20}$$

where $\Delta\theta$ provides a measure of the width of the peak and, hence, of the mosaic spread in the crystal.

2.5. *Figure of merit*

Suppose, on the other hand, that we have a collimated polyenergetic incident beam of neutrons that makes an angle θ_0 with the Bragg planes. It then follows from (12) that

$$J'(\theta_0)/J = \varsigma \int_0^\infty R(\theta_0, \lambda) f(\lambda)\,\mathrm{d}\lambda. \tag{21}$$

Here, $R(\theta_0, \lambda)$ is sharply peaked at $\lambda = \lambda_0$ while $f(\lambda)$ is a slowly varying function of λ that is essentially constant over this peak. Hence,

$$J'(\theta_0)/J = Mf(\lambda_0), \tag{22}$$

where

$$M = \varsigma\rho(\theta_0) \tag{23}$$

and

$$\rho(\theta_0) = \int R(\theta_0, \lambda)\,\mathrm{d}\lambda = R_0\,\Delta\lambda. \tag{24}$$

In this equation, R_0 is the peak reflectivity (19) as before and $\Delta\lambda$ provides a measure of the wavelength spread in the Bragg reflected beam.

In can be shown that, to a good approximation, the reflectivity $R(\theta, \lambda)$ does not depend on θ and λ separately but only on the difference $\lambda - \lambda_{\max}\sin\theta$. It then follows that

$$\rho(\theta_0) = \lambda_0 \cot\theta_0\,\rho(\lambda_0) \tag{25}$$

and, hence, that

$$\Delta\lambda = \lambda_0 \cot\theta_0\,\Delta\theta. \tag{26}$$

The flux ratio (22) is the product of a factor M, which depends only on the crystal, and a factor $f(\lambda_0)$, which depends only on the incident beam. The quantity M will therefore be called the figure of merit of the crystal for the particular reflection under consideration and can be expressed in the alternative form

$$M = \varsigma R_0\,\Delta\lambda. \tag{27}$$

2.6. *Incident-neutron spectrum*

For a hypothetical source in which the neutrons are in true thermodynamic equilibrium at temperature T, the velocity distribution of the neutrons is Maxwellian and (Bacon & Thewlis, 1949)

$$f(\lambda) = (2\lambda_T^4/\lambda^5)\exp[-(\lambda_T/\lambda)^2]. \tag{28}$$

Here, λ_T denotes the wavelength of a neutron with energy k_BT so that

$$\lambda_T = h/(2mk_BT)^{1/2}, \tag{29}$$

where m is the neutron mass. The incident-neutron spectrum $f(\lambda)$ is then a maximum when $\lambda = (2/5)^{1/2}\lambda_T$.

The neutrons in a nuclear reactor are not in true thermodynamic equilibrium with the moderator. Nevertheless, the velocity distribution of the neutrons is found to be very nearly Maxwellian up to energies of about $5k_BT$ (Westcott, 1955) and the effective neutron temperature in a heavy-water reactor is typically 10 to 30 K higher than the temperature of the moderator (Johansson, Lampa & Sjöstrand, 1961; Bigham, Chidley & Turner, 1961). Thus, $f(\lambda)$ is well represented by expression (28) for wavelengths $\lambda > \lambda_T/5^{1/2}$. In the short-wavelength (epithermal) region, where the neutrons are still slowing down, the incident-neutron flux is inversely proportional to the energy (Fermi, 1936) so that

$$f(\lambda) = \text{constant}/\lambda, \quad \lambda < \lambda_T/5^{1/2}, \tag{30}$$

and this is larger than would be expected on the basis of (28). In practice, the incident beam is often filtered to suppress the epithermal tail as much as possible in order to minimize the order contamination in the Bragg reflected beam.

2.7. *Real monochromators*

The above results are idealized in a number of important respects. Firstly, we shall assume later in this paper that the reflectivity can be calculated from the solution of the Darwin equations given in I. This requires a spatially homogeneous mosaic structure, which is usually not realized very well in actual monochromator crystals (Dorner, 1971; Schneider, 1974; Freund, 1975, 1985). It also requires that the widths of both the crystal and the incident beam are effectively infinite. The effect of finite beam width on the reflecting properties of monochromator crystals has been discussed earlier (Werner & Arrott, 1965; Werner, Arrott, King & Kendrick, 1966).

We shall treat the 'mosaic spread' $\Delta\theta$ as a constant, which it is if one uses the simple model for $W(\theta'-\theta)$ given by (57) in I. More generally, the quantity $\Delta\theta$, as defined by (20), is roughly proportional to the actual mosaic spread in the crystal but it also depends to some extent on the wavelength and the thickness of the crystal.

We also assume an ideally collimated incident beam. In practice, the incident beam always has a small but finite angular divergence, which changes the effective reflectivity of the crystal. Methods of correcting for this effect have been discussed by Dietrich & Als-Neilsen (1965) and by Popovici, Gheorghiu & Gelberg (1969).

For some wavelengths, Bragg's law may be satisfied for two or more sets of Bragg planes simultaneously and the additional parasitic reflections have the effect of reducing the intensity of the desired reflection by several percent at these wavelengths (Blinowski & Sosnowski, 1961; Moon & Shull, 1964; Prager, 1971).

Finally, owing to the difficulty and expense of producing large single crystals with spatially homogeneous microstructures, actual monochromators are now often made in the form of composite arrays or stacks of many crystals (Freund, 1975; Vogt, Passell, Cheung & Axe, 1994). While the various complications mentioned above are often important in practice, they can be ignored in answering the kinds of generic questions that concern us in the present paper.

3. Symmetric reflections

We begin with a discussion of symmetric reflections (Fig. 1), where the Bragg planes are either parallel or perpendicular to the surface of the crystal. We shall illustrate our results with particular reference to the Si 111 reflection. Unless stated otherwise, the calculations assume a crystal thickness $d = 1.0\,\text{cm}$ and a mosaic spread $\Delta\theta = 0.3°$.

3.1. *Bragg reflection and attenuation coefficients*

Table 1 lists the values of some quantities for a number of common neutron monochromator crystals. These quantities determine the Bragg reflection coefficient σ and the attenuation coefficient μ, and hence the reflectivity of the crystal, as discussed in I. For example, Fig. 2 shows the calculated values of σ (solid curve) and μ (dashed curve) for silicon as a function of wavelength. The values of σ are calculated at the center of the Bragg peak for the 111 reflection and assume a mosaic spread $\Delta\theta = 0.3°$. Fig. 3 shows the individual contributions of coherent inelastic scattering and absorption to the total attenuation coefficient for silicon. The contribution from incoherent scattering has a constant value of $0.0002\,\text{cm}^{-1}$, which is negligibly small on the scale of Fig. 3.

For wavelengths $\lambda \gg 1\,\text{Å}$, we see in Figs. 2 and 3 that $\sigma \gg \mu$ and the attenuation is mainly due to absorption. When $\lambda \simeq 1\,\text{Å}$, we have $\sigma \simeq \mu$ and, when $\lambda \ll 1\,\text{Å}$, we have $\sigma \ll \mu$. Below 1 Å, the attenuation is mainly due to coherent inelastic scattering. This behavior of σ and μ at short wavelengths is true quite generally and allows the use of single-crystal filters to remove the epithermal neutrons from the incident beam (Brockhouse, 1959; Sears, 1989).

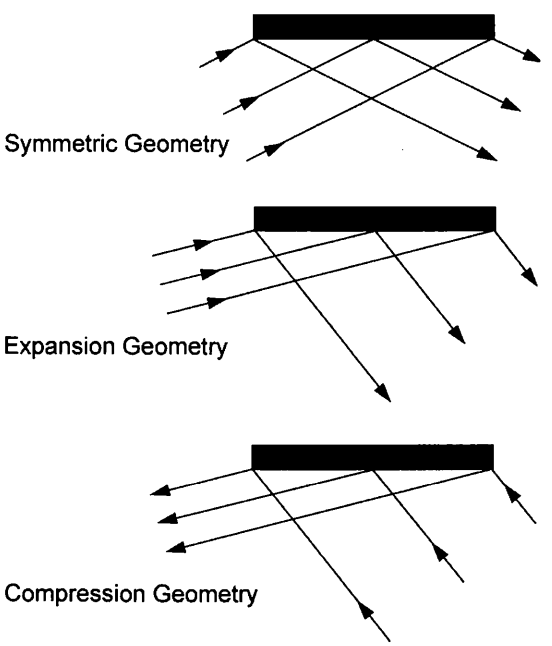

Fig. 1. Bragg reflection from a plane slab. Illustration of symmetric, expansion and compression geometries in the Bragg case.

Table 1. *Quantities that determine the reflecting properties of various neutron monochromator crystals*

a and c are the lattice constants, u_0 is the root-mean-square displacement of an atom perpendicular to the Bragg planes, b_c the bound coherent scattering length, σ_c the bound coherent scattering cross section, σ_i the bound incoherent scattering cross section, σ_a the absorption cross section at $\lambda = 1.798\,\text{Å}$ and PG denotes pyrolytic graphite. (1 barn = 100 fm^2.)

	Al	Cu	Ge	Si	Be	PG
Structure	F.c.c.	F.c.c.	Diamond	Diamond	H.c.p.	Hexagonal layer
a (Å)	4.0495	3.6147	5.6575	5.4309	2.2856	2.461
c (Å)					3.5832	6.708
u_0 (Å)	0.101	0.084	0.088	0.081	0.081	0.33*
b_c (fm)	3.449	7.718	8.185	1.1491	7.79	6.6460
σ_c (barn)	1.495	7.485	8.42	2.1633	7.63	5.550
σ_i (barn)	0.0082	0.55	0.18	0.004	0.0018	0.001
σ_a (barn)	0.231	3.78	2.20	0.171	0.0076	0.00350

*For displacements parallel to the c axis.

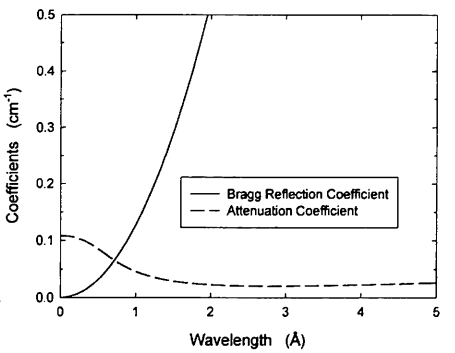

Fig. 2. The Bragg reflection coefficient σ and the attenuation coefficient μ for silicon as a function of wavelength. The values of σ are calculated at the center of the Bragg peak for the 111 reflection with $\Delta\theta = 0.3°$.

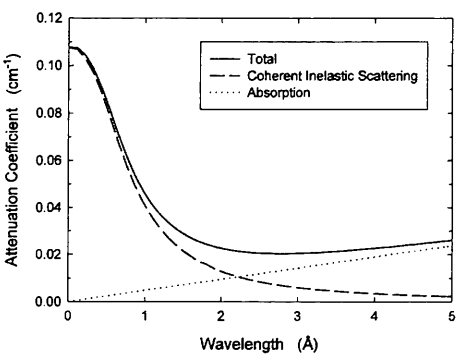

Fig. 3. Contributions of coherent inelastic scattering and absorption to the total attenuation coefficient μ for silicon. The contribution from incoherent scattering is negligible in silicon.

3.2. *Peak reflectivity*

Fig. 4 shows the peak reflectivity of the Si 111 reflection for the symmetric Bragg and Laue cases as a function of wavelength for a crystal thickness $d = 1.0\,\text{cm}$. As $\lambda \to \lambda_{\max}$ in the Laue case, the path lengths of the incident and Bragg-reflected beams inside the crystal become infinite and the resulting attenuation causes the reflectivity to fall rapidly to zero.

In Figs. 5 and 6, the peak reflectivity for this reflection is shown as a function of crystal thickness for wavelengths of 1, 2, 3 and 4 Å. For the symmetric Bragg case, we see in Fig. 5 that the reflectivity approaches a saturation value R_∞ as $d \to \infty$ and the value of R_∞ increases with increasing wavelength. In the symmetric Laue case (Fig. 6), the reflectivity at each wavelength increases initially with increasing thickness until it reaches a maximum value beyond which it falls slowly to zero as $d \to \infty$. The position of the maximum is the optimum thickness, which is discussed further in §3.4.

Table 2 lists the maximum wavelength $\lambda_{\max}$ and the saturation reflectivity of various monochromator reflection planes for wavelengths $\lambda = 1, 2, 3$ and 4 Å. For a given crystal, the value of R_∞ usually depends more strongly on λ than it does on (hkl).

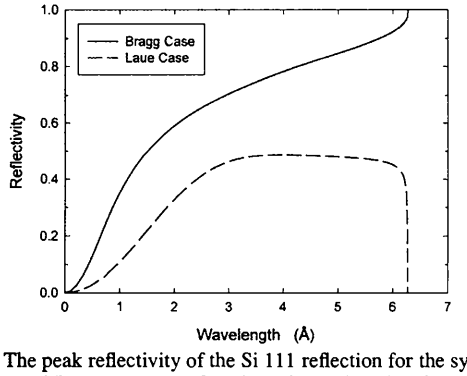

Fig. 4. The peak reflectivity of the Si 111 reflection for the symmetric Bragg and Laue cases as a function of wavelength. The curves are calculated for $d = 1.0\,\text{cm}$ and $\Delta\theta = 0.3°$.

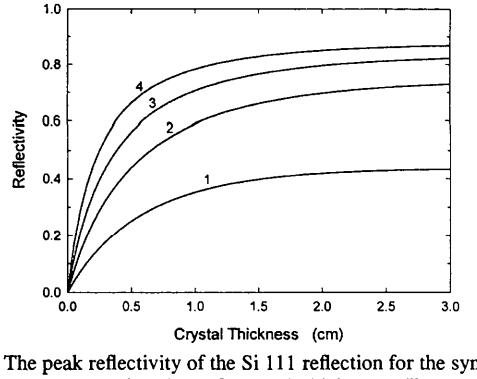

Fig. 5. The peak reflectivity of the Si 111 reflection for the symmetric Bragg case as a function of crystal thickness. The curves are calculated for $\lambda = 1, 2, 3$ and 4 Å with $\Delta\theta = 0.3°$.

Table 2. *Maximum wavelength λ_{max} (Å) and saturation reflectivity R_∞ of various monochromator reflection planes*

The values of R_∞ are calculated for the symmetric Bragg case from equation (35) in I for wavelengths $\lambda = 1, 2, 3$ and 4 Å. The mosaic spread $\Delta\theta = 0.3°$ for all reflections.

		R_∞			
Planes	$\lambda_{\max}$	1	2	3	4
Al (111)	4.676	0.474	0.754	0.842	0.892
Al (200)	4.050	0.447	0.740	0.839	0.934
Al (220)	2.863	0.376	0.711		
Al (311)	2.442	0.341	0.709		
Cu (111)	4.174	0.475	0.696	0.784	0.876
Cu (200)	3.615	0.449	0.682	0.789	
Cu (220)	2.556	0.382	0.663		
Cu (311)	2.180	0.351	0.692		
Ge (111)	6.533	0.367	0.641	0.734	0.784
Ge (220)	4.000	0.397	0.675	0.781	0.969
Ge (311)	3.412	0.254	0.556	0.722	
Ge (400)	2.829	0.331	0.645		
Si (111)	6.271	0.438	0.747	0.837	0.877
Si (220)	3.840	0.469	0.775	0.870	
Si (311)	3.275	0.322	0.684	0.841	
Si (400)	2.715	0.404	0.756		
Be (100)	3.959	0.411	0.783	0.907	
Be (002)	3.583	0.619	0.880	0.954	
Be (101)	3.465	0.570	0.862	0.948	
Be (110)	2.286	0.542	0.879		
PG (002)	6.708	0.510	0.738	0.846	0.905

3.3. *Figure of merit*

The figure of merit M is the most important property of a monochromator crystal because it is this quantity that determines the magnitude of the reflected-neutron flux. Fig. 7 shows the values of M calculated from (27) as a function of wavelength for the Si 111 reflection in the symmetric Bragg and Laue cases. The $\cot\theta_0$ factor in (26) makes $\Delta\lambda$ and, hence, M vanish at the maximum wavelength where $\theta_0 = 90°$.

3.4. *Optimum crystal thickness*

Fig. 8 shows the optimum crystal thickness d_{opt} of the Si 111 reflection for the symmetric Bragg and Laue

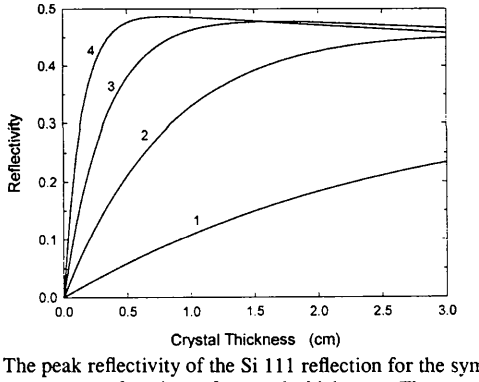

Fig. 6. The peak reflectivity of the Si 111 reflection for the symmetric Laue case as a function of crystal thickness. The curves are calculated for $\lambda = 1, 2, 3$ and 4 Å with $\Delta\theta = 0.3°$.

cases as a function of wavelength. In the Bragg case, d_{opt} is taken to be the thickness at which the peak reflectivity reaches 80% of its saturation value and, in the Laue case, d_{opt} is the thickness at which the peak reflectivity is a maximum (see Fig. 6). Note that the values of d_{opt} for the Bragg and Laue cases are roughly the same at 4 Å but d_{opt} is very much larger for the Laue case at 1 Å.

The values of d_{opt} for various monochromator reflection planes are listed in Table 3 for the symmetric Bragg case and in Table 4 for the symmetric Laue case, for wavelengths $\lambda = 1, 2, 3$ and 4 Å.

3.5. *Incident and reflected neutron flux*

Fig. 9 shows the assumed incident-neutron flux as a function of wavelength. The dashed curve is for an equilibrium incident-neutron spectrum with an effective neutron temperature $T = 310$ K and the solid curve shows the result of including the epithermal tail. Experiments show that this tail begins rather abruptly at an energy of about $5k_BT$ (Westcott, 1955). For simplicity, we assume that it begins at $5k_BT$ exactly. According to (29), the parameter $\lambda_T = 1.75$ Å at 310 K.

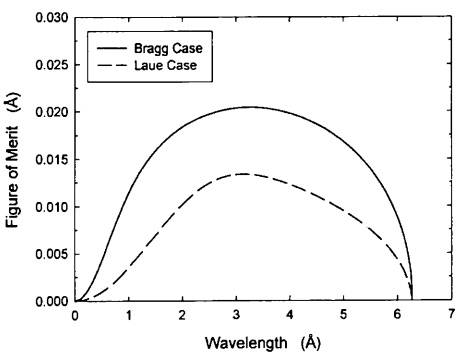

Fig. 7. The figure of merit M of the Si 111 reflection for the symmetric Bragg and Laue cases as a function of wavelength. The curves are calculated for $d = 1.0$ cm and $\Delta\theta = 0.3°$.

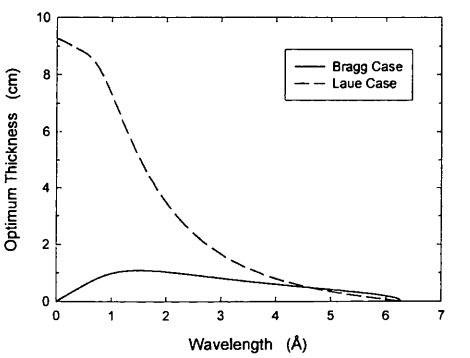

Fig. 8. The optimum crystal thickness for the Si 111 reflection in the symmetric Bragg and Laue cases as a function of wavelength. The curves are calculated for $\Delta\theta = 0.3°$.

Table 3. *Optimum crystal thickness d_{opt} (cm) for various monochromator reflection planes calculated from equation (41) in I with $x = 0.8$ for the symmetric Bragg case with wavelengths $\lambda = 1$, 2, 3 and 4 Å*

The mosaic spread $\Delta\theta = 0.3°$ for all reflections.

Planes	1	2	3	4
Al (111)	1.006	0.945	0.681	0.404
Al (200)	1.267	1.198	0.809	0.192
Al (220)	2.202	2.021		
Al (311)	2.839	2.389		
Cu (111)	0.126	0.099	0.066	0.027
Cu (200)	0.158	0.124	0.073	
Cu (220)	0.272	0.193		
Cu (311)	0.349	0.194		
Ge (111)	0.242	0.242	0.190	0.145
Ge (220)	0.363	0.335	0.224	0.007
Ge (311)	0.618	0.661	0.391	
Ge (400)	0.615	0.549		
Si (111)	0.983	1.039	0.820	0.608
Si (220)	1.458	1.401	0.898	
Si (311)	2.609	2.904	1.493	
Si (400)	2.512	2.267		
Be (100)	0.217	0.253	0.184	
Be (002)	0.115	0.100	0.057	
Be (101)	0.145	0.133	0.073	
Be (110)	0.245	0.160		
PG (002)	0.056	0.048	0.040	0.033

Hence, the incident-neutron flux is a maximum at $\lambda = 1.11$ Å and the epithermal tail begins at $\lambda = 0.78$ Å.

Fig. 10 shows the corresponding reflected-neutron flux for the Si 111 reflection in the symmetric Bragg case. According to (22), the reflected-neutron flux is proportional to the product of the figure of merit and the incident-neutron flux. It is seen in Fig. 7 that, in the range 1 to 5 Å (say), the figure of merit varies rather slowly with wavelength. As a result, the reflected-neutron flux distribution in this region is roughly similar in shape to the incident-neutron flux. In the epithermal region, on the other hand, the figure of merit is approximately proportional to λ^2 and the incident-neutron flux is proportional to $1/\lambda$, so that the reflected-neutron flux varies more or less linearly with λ.

For a liquid-hydrogen cold source with an effective neutron temperature $T = 20$ K, we find that

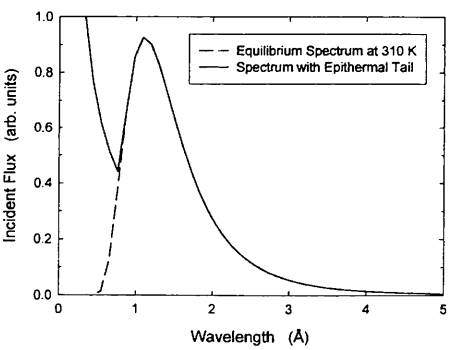

Fig. 9. The incident-neutron flux as a function of wavelength.

Table 4. *Optimum crystal thickness d_{opt} (cm) for various monochromator reflection planes calculated from equation (40) in I for the symmetric Laue case with wavelengths $\lambda = 1$, 2, 3 and 4 Å*

The mosaic spread $\Delta\theta = 0.3°$ for all reflections.

Planes	1	2	3	4
Al (111)	5.490	2.239	0.896	0.269
Al (200)	5.963	2.373	0.807	0.034
Al (220)	7.163	2.347		
Al (311)	7.703	1.898		
Cu (111)	0.610	0.207	0.071	0.009
Cu (200)	0.659	0.213	0.055	
Cu (220)	0.776	0.176		
Cu (311)	0.822	0.096		
Ge (111)	1.895	0.869	0.414	0.208
Ge (220)	1.700	0.664	0.220	0.0001
Ge (311)	2.478	1.074	0.239	
Ge (400)	1.984	0.632		
Si (111)	7.313	3.468	1.656	0.806
Si (220)	6.462	2.561	0.787	
Si (311)	9.930	4.298	0.719	
Si (400)	7.658	2.333		
Be (100)	1.002	0.480	0.175	
Be (002)	0.458	0.163	0.043	
Be (101)	0.565	0.206	0.048	
Be (110)	0.594	0.097		
PG (002)	0.441	0.173	0.089	0.048

$\lambda_T = 6.89$ Å. Hence, the incident-neutron flux is a maximum at $\lambda = 4.36$ Å. Apart from a shift to longer wavelengths, the reflected-neutron flux for a cold source is qualitatively similar to that for a thermal source.

3.6. *Order contamination*

Two examples of order contamination in silicon for the symmetric Bragg case are illustrated in Fig. 11. The curves show the reflected-flux ratios for 440/220 and 333/111 as functions of wavelength. In each case, the dashed curve is for an equilibrium incident-neutron spectrum with an effective neutron temperature of 310 K and the solid curve shows the result of including the epithermal tail (see Fig. 9). Note that the second-order reflection 222 is forbidden in a crystal with the diamond structure such as silicon, so that the lowest-order contaminant is 333.

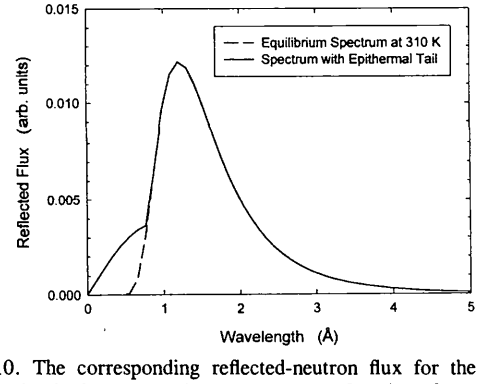

Fig. 10. The corresponding reflected-neutron flux for the Si 111 reflection in the symmetric Bragg case as a function of wavelength. The curves are calculated for $d = 1.0$ cm and $\Delta\theta = 0.3°$.

In general, the reflected-flux ratio for an nth-order contaminant is given, according to (22), by

$$(M_n/M_1)\, f(\lambda/n)/f(\lambda), \tag{31}$$

in which M_n is the figure of merit for the nth-order reflection and M_1 the figure of merit for the primary reflection, whose wavelength is λ. The ratio of the figures of merit in (31) varies relatively slowly with wavelength so that the behavior of the curves in Fig. 11 is mainly determined by the ratio of the incident-neutron flux at the two wavelengths.

4. Asymmetric reflections

We now discuss asymmetric reflections (Fig. 1), where the Bragg planes make an angle α with the surface of the crystal. We then have the Laue case when $\theta < \alpha$ and the Bragg case when $\theta > \alpha$. The Fankuchen limit ($\theta = \alpha$) occurs at the wavelength

$$\lambda_F = \lambda_{\max} \sin\alpha. \tag{32}$$

We shall again illustrate our results with particular reference to the Si 111 reflection. Unless stated otherwise, the calculations assume a crystal thickness $d = 1.0$ cm and a mosaic spread $\Delta\theta = 0.3°$.

4.1. *Peak reflectivity*

Fig. 12 shows the peak reflectivity of the Si 111 reflections as a function of wavelength for the symmetric Bragg case (where $\alpha = 0°$), and for asymmetric reflections (with $\alpha = 20°$) in both compression and expansion geometries (see Appendix *A*1 in I for a discussion of these terms). For $\alpha = 20°$, the Fankuchen

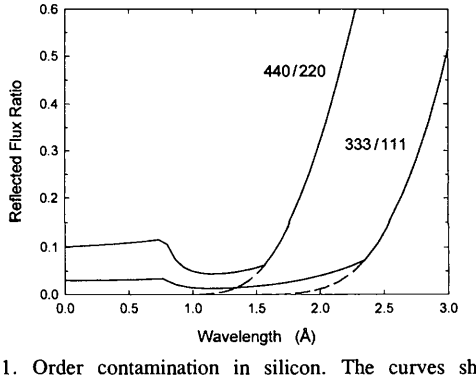

Fig. 11. Order contamination in silicon. The curves show the reflected-flux ratios for 440/220 and 333/111 as functions of wavelength. In each case, the dashed curve is for an equilibrium incident-neutron spectrum with an effective neutron temperature of 310 K and the solid curve shows the result of including the epithermal tail (Fig. 9). The curves are calculated for the symmetric Bragg case with $d = 1.0$ cm and $\Delta\theta = 0.3°$.

wavelength $\lambda_F = 2.145$ Å and we have the Laue case when $\lambda < \lambda_F$ and the Bragg case when $\lambda > \lambda_F$.

The peak reflectivity for the Si 111 reflection in compression geometry is shown as a function of α in Fig. 13. The curves are calculated for wavelengths $\lambda = 1, 2, 3$ and 4 Å as indicated. Note that, as in Fig. 12, the reflectivity vanishes when $\lambda_F = \lambda$. As discussed in I, this behavior arises because the Fankuchen factor $\varsigma \to \infty$ when $\theta = \alpha$ and $\lambda = \lambda_F$, while $\varsigma R \leq 1$ always.

4.2. *Figure of merit*

The Fankuchen factor ς for the Si 111 reflection is shown in Fig. 14 as a function of wavelength when $\alpha = 20°$. Results are shown for compression geometry ($\varsigma > 1$), expansion geometry ($\varsigma < 1$) and symmetric geometry ($\varsigma = 1$). Note that, as stated in the preceding section, for compression geometry, $\varsigma \to \infty$ as $\lambda \to \lambda_F$.

Fig. 15 shows the figure of merit M for the Si 111 reflection as a function of wavelength for the symmetric Bragg case (where $\alpha = 0°$) and for asymmetric reflections (with $\alpha = 20°$) in both compression and expansion geometries. The figure of merit for this reflection is shown as a function of α in Fig. 16 for compression geometry. The curves are calculated for wavelengths $\lambda = 1, 2, 3$ and 4 Å as indicated.

Comparing Figs. 12 and 15, we see that the reflectivity is smaller for compression geometry while the figure of merit (and, hence, the reflected-neutron

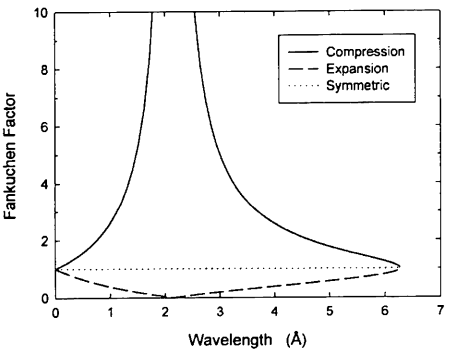

Fig. 14. The Fankuchen factor ς for the Si 111 reflection as a function of wavelength when $\alpha = 20°$. Results are shown for compression geometry ($\varsigma > 1$), expansion geometry ($\varsigma < 1$) and symmetric geometry ($\varsigma = 1$).

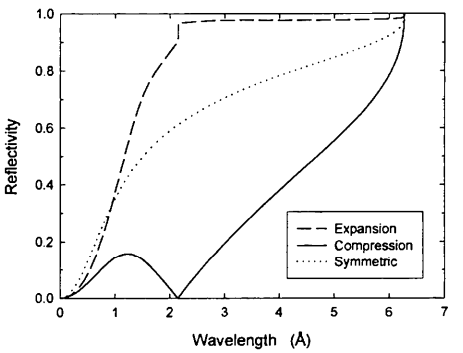

Fig. 12. The peak reflectivity of the Si 111 reflection as a function of wavelength for the symmetric Bragg case (where $\alpha = 0°$) and for asymmetric reflctions (with $\alpha = 20°$) in both compression and expansion geometries. The curves are calculated for $d = 1.0$ cm and $\Delta\theta = 0.3°$.

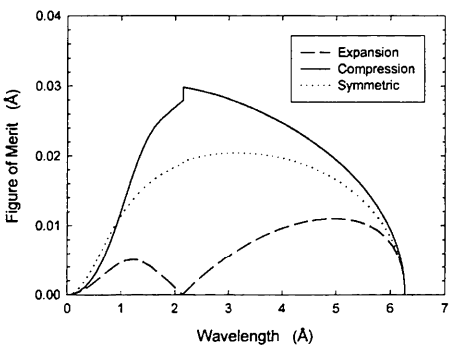

Fig. 15. The figure of merit M for the Si 111 reflection as a function of wavelength for the symmetric Bragg case (where $\alpha = 0°$) and for asymmetric reflections (with $\alpha = 20°$) in both compression and expansion geometries. The curves are calculated for $d = 1.0$ cm and $\Delta\theta = 0.3°$.

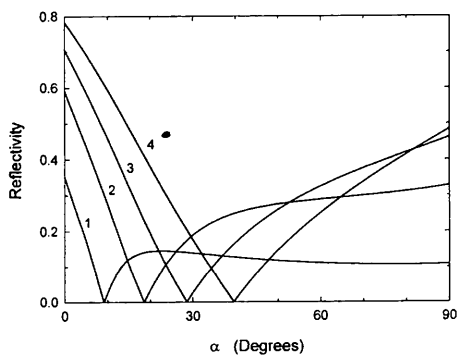

Fig. 13. The peak reflectivity for the Si 111 reflection in compression geometry as a function of α. The curves are calculated for $\lambda = 1, 2, 3$ and 4 Å with $d = 1.0$ cm and $\Delta\theta = 0.3°$.

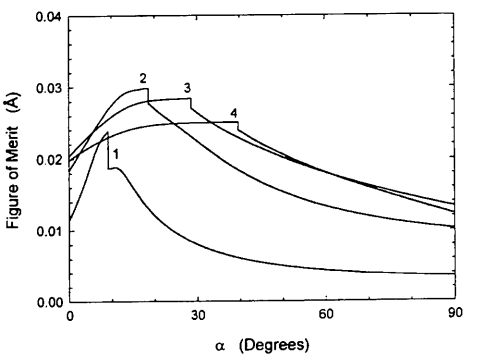

Fig. 16. The figure of merit M for the Si 111 reflection in compression geometry as a function of α. The curves are calculated for $\lambda = 1, 2, 3$ and 4 Å with $d = 1.0$ cm and $\Delta\theta = 0.3°$.

flux) is larger. Furthermore, for compression geometry, the figure of merit is largest at the Fankuchen wavelength λ_F where the reflectivity vanishes. The discontinuity in the figure of merit at λ_F is due to the effect of attenuation. If $\mu = 0$, this discontinuity vanishes, leaving only a cusp in this quantity at λ_F (see §5.3 in I).

4.3. *Fankuchen gain*

As discussed in I, the Fankuchen gain is defined by the reflected-flux ratio

$$G = J'(\theta)/J'(\theta)_s = M/M_s = \varsigma R/R_s, \qquad (33)$$

where the quantities in the numerators refer to the situation where the Bragg planes are at an angle α to the surface of the crystal and the quantities in the denominators refer to the corresponding symmetric reflection where $\alpha = 0$ and $\varsigma = 1$.

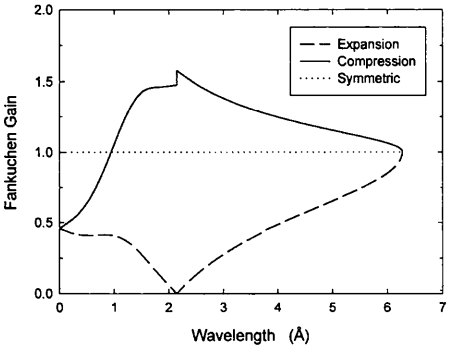

Fig. 17. The Fankuchen gain G for the Si 111 reflection as a function of wavelength for the symmetric Bragg case (where $\alpha = 0°$) and for asymmetric reflections (with $\alpha = 20°$) in both compression and expansion geometries. The curves are calculated for $d = 1.0$ cm and $\Delta\theta = 0.3°$.

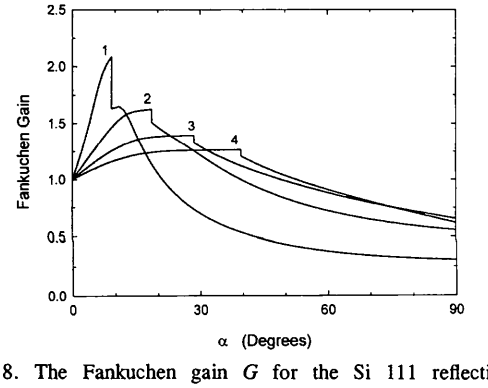

Fig. 18. The Fankuchen gain G for the Si 111 reflection in compression geometry as a function of α. The curves are calculated for $\lambda = 1, 2, 3$ and 4 Å with $d = 1.0$ cm and $\Delta\theta = 0.3°$.

Fig. 17 shows the Fankuchen gain G for the Si 111 reflection as a function of wavelength for the symmetric Bragg case (where $\alpha = 0°$), and for asymmetric reflections (with $\alpha = 20°$) in both compression and expansion geometries. The gain for compression geometry is shown as a function of α in Fig. 18, and the curves are calculated for wavelengths $\lambda = 1, 2, 3$ and 4 Å as indicated. The discontinuity in G for compression geometry occurs where $\lambda = \lambda_F$ and the reflected beam is parallel to the surface of the crystal. Below the discontinuity, we have the Laue case and above it the Bragg case. It is evident that gains in flux of 25 to 50% or more can easily be achieved for a wide range of wavelengths. Note also that the value of G can exceed the value 2, which is the conventional upper limit for X-rays (see the discussion in §6 of I). Finally, it is seen that at each wavelength there is a maximum angle α_{max} such that $G > 1$ only if $\alpha < \alpha_{max}$ and the value of α_{max} increases with increasing λ.

References

Bacon, G. E. & Thewlis, J. (1949). *Proc. R. Soc. London Ser. A*, **196**, 50–64.
Bigham, C. B., Chidley, B. G. & Turner, R. B. (1961). Report AECL-1350. Atomic Energy of Canada Limited, Chalk River, Ontario, Canada.
Blinowski, K. & Sosnowski, J. (1961). *Nucl. Instrum. Methods*, **10**, 289–294.
Brockhouse, B. N. (1959). *Rev. Sci. Instrum.* **30**, 136–137.
Dietrich, O. W. & Als-Nielsen, J. (1965). *Acta Cryst.* **18**, 184–188.
Dorner, B. (1971). *J. Appl. Cryst.* **4**, 185–190.
Fermi, E. (1936). *Ric. Sci.* **7**, 13–52.
Freund, A. K. (1975). *Nucl. Instrum. Methods*, **124**, 93–99.
Freund, A. K. (1985). *Nucl. Instrum. Methods*, **A238**, 570–571.
Johansson, E., Lampa, E. & Sjöstrand, N. G. (1961). *Ark. Fys.* **18**, 513–531.
Moon, R. M. & Shull, C. G. (1964). *Acta Cryst.* **17**, 805–812.
Popovici, M., Gheorghiu, Z. & Gelberg, D. (1969). *Nucl. Instrum. Methods*, **69**, 125–130.
Prager, P. R. (1971). *Acta Cryst.* **A27**, 563–569.
Schneider, J. R. (1974). *J. Appl. Cryst.* **7**, 541–546, 547–554.
Sears, V. F. (1989). *Neutron Optics*. New York: Oxford University Press.
Sears, V. F. (1997). *Acta Cryst.* **A53**, 35–45.
Vogt, T., Passell, L., Cheung, S. & Axe, J. D. (1994). *Nucl. Instrum. Methods*, **A338**, 71–77.
Werner, S. A. & Arrott, A. (1965). *Phys. Rev.* **140**, A675–A686.
Werner, S. A., Arrott, A., King, J. S. & Kendrick, H. (1966). *J. Appl. Phys.* **37**, 2343–2350.
Westcott, C. H. (1955). *J. Nucl. Energy*, **2**, 59–76.